THE ASTROPHYSICAL JOURNAL, 550:75–86, 2001 March 20


# EVIDENCE OF A SUPERMASSIVE BLACK HOLE IN THE GALAXY NGC 1023 FROM THE NUCLEAR STELLAR DYNAMICS[1]

G. A. BOWER,[2] R. F. GREEN,[2] R. BENDER,[3] K. GEBHARDT,[4] T. R. LAUER,[2] J. MAGORRIAN,[5] D. O. RICHSTONE,[6] A. DANKS,[7] T. GULL,[8] J. HUTCHINGS,[9] C. JOSEPH,[10] M. E. KAISER,[11] D. WEISTROP,[12] B. WOODGATE,[8] C. NELSON,[12] AND E. M. MALUMUTH[7]

*Received 2000 August 29; accepted 2000 November 21*

## ABSTRACT

We analyze the nuclear stellar dynamics of the SB0 galaxy NGC 1023, utilizing observational data both from the Space Telescope Imaging Spectrograph aboard the *Hubble Space Telescope* and from the ground. The stellar kinematics measured from these long-slit spectra show rapid rotation ($V \approx 70$ km s$^{-1}$ at a distance of $0''.1 = 4.9$ pc from the nucleus) and increasing velocity dispersion toward the nucleus (where $\sigma = 295 \pm 30$ km s$^{-1}$). We model the observed stellar kinematics assuming an axisymmetric mass distribution with both two and three integrals of motion. Both modeling techniques point to the presence of a central dark compact mass (which presumably is a supermassive black hole) with confidence greater than 99%. The isotropic two-integral models yield a best-fitting black hole mass of $(6.0 \pm 1.4) \times 10^7\ M_\odot$ and mass-to-light ratio ($M/L_V$) of $5.38 \pm 0.08$, and the goodness of fit ($\chi^2$) is insensitive to reasonable values for the galaxy's inclination. The three-integral models, which nonparametrically fit the observed line-of-sight velocity distribution as a function of position in the galaxy, suggest a black hole mass of $(3.9 \pm 0.4) \times 10^7\ M_\odot$ and $M/L_V$ of $5.56 \pm 0.02$ (internal errors), and the edge-on models are vastly superior fits over models at other inclinations. The internal dynamics in NGC 1023 as suggested by our best-fit three-integral model shows that the velocity distribution function at the nucleus is tangentially anisotropic, suggesting the presence of a nuclear stellar disk. The nuclear line-of-sight velocity distribution has enhanced wings at velocities $\geq 600$ km s$^{-1}$ from systemic, suggesting that perhaps we have detected a group of stars very close to the central dark mass.

*Subject headings:* galaxies: elliptical and lenticular, cD — galaxies: individual (NGC 1023) — galaxies: kinematics and dynamics — galaxies: nuclei

## 1. INTRODUCTION

Supermassive black holes (BHs) are widely suspected to be the central engines of quasars and active galactic nuclei. The fact that the comoving number density of quasars peaks at $z \sim 2$–3 (e.g., Schmidt, Schneider, & Gunn 1995) and declines by nearly 3 orders of magnitude by $z = 0$ implies that nearby galaxies should harbor relatively inactive BHs. Searching for these BHs would provide constraints on the evolutionary history of quasars. Also, the most recent census of nearby BHs reveals a remarkable correlation between BH mass and the stellar velocity dispersion measured within the half-light radius of its host galaxy (Gebhardt et al. 2000a; Ferrarese & Merritt 2000). This result will have very interesting implications for the formation of galaxy spheroids and the growth of their central BHs (Kormendy 2000).

Dynamical evidence of dark compact objects of mass $\sim 10^{6.5}$–$10^{9.5}\ M_\odot$ has been accumulating rapidly in the last decade or so (see reviews in Kormendy & Richstone 1995; Richstone et al. 1998). Although this evidence in most cases does not strictly exclude alternatives to a BH, it is very difficult to construct plausible alternative models to BHs for three of these BH candidates (the Galaxy, NGC 4258, and M31; see Maoz 1998 and Kormendy & Bender 1999)—thus suggesting that many, or perhaps all, of the dark compact objects that have been identified through such dynamical evidence are indeed BHs.

The *Hubble Space Telescope* (*HST*) has greatly enhanced this effort to analyze the nuclear dynamics of nearby galaxies. *HST*'s second-generation spectrograph, the Space Telescope Imaging Spectrograph (STIS; see Woodgate et al. 1998), can obtain measurements of the nuclear kinematics of either gas or stars with much more efficiency than the first-generation *HST* spectrographs.

Several teams are actively involved in this research. Our group, a subset of the STIS Investigation Definition Team, has selected a galaxy sample including both some of the best black hole candidates and a few galaxies where the ground-based dynamical evidence for a BH is nonexistent or weak.

[1] Based on observations with the NASA/ESA *Hubble Space Telescope*, obtained at the Space Telescope Science Institute, which is operated by the Association of Universities for Research in Astronomy, Inc. (AURA), under NASA contract NAS 5-26555.

[2] Kitt Peak National Observatory, National Optical Astronomy Observatories, P.O. Box 26732, Tucson, AZ 85726; gbower@noao.edu, operated by AURA, Inc., under cooperative agreement with the National Science Foundation.

[3] Universitäts-Sterwarte, Scheinerstrasse 1, D-81679 München, Germany.

[4] Department of Astronomy, University of Texas at Austin, Austin, TX 78712.

[5] Institute of Astronomy, Cambridge University, Madingley Road, Cambridge, CB3 0HA, England.

[6] Department of Astronomy, University of Michigan, Dennison Building, Ann Arbor, MI 48109.

[7] Raytheon ITSS, NASA Goddard Space Flight Center, Code 681, Greenbelt, MD 20771.

[8] NASA Goddard Space Flight Center, Code 681, Greenbelt, MD 20771.

[9] Dominion Astrophysical Observatory, National Research Council of Canada, 5071 West Saanich Road, Victoria, BC V8X 4M6, Canada.

[10] Department of Physics and Astronomy, Rutgers University, P.O. Box 849, Piscataway, NJ 08855.

[11] Department of Physics and Astronomy, Johns Hopkins University, Homewood Campus, Baltimore, MD 21218.

[12] Department of Physics, University of Nevada, 4505 South Maryland Parkway, Las Vegas, NV 89154.

One such galaxy in the latter category is NGC 1023, which is classified as SB(rs)0−. Given this morphological type and that $M_B = -19.9$, the luminosity of the bulge component is $M_{B,\mathrm{bulge}} \approx -19.4$ (see Simien & de Vaucouleurs 1986). We chose NGC 1023 because its intermediate luminosity is consistent with a rotationally supported figure (Faber et al. 1997), removing ambiguity from the interpretation of the nuclear dynamics.

We adopt a distance of 10.2 Mpc (see Faber et al. 1997); thus 1″ corresponds to a distance at NGC 1023 of 49 pc. The Galactic extinction is $A_B = 0.262$ mag (Schlegel et al. 1998).

## 2. OBSERVATIONS AND DATA CALIBRATION

Analyzing the nuclear stellar dynamics of galaxies requires imaging and spectroscopy using both *HST* and ground-based observations. *HST* observations measure the galactic central structure and stellar kinematics within a distance of a few arcseconds of the nucleus where the radial gradients in intensity and kinematics are steepest. Ground-based observations extend the spatial coverage to large radius so that the global photometric and kinematic structure of the galaxy can be fitted during construction of galaxy dynamical models.

### 2.1. *Surface Photometry*

Continuum images of the nuclear region of NGC 1023 were obtained with the Wide Field Planetary Camera 2 (WFPC2) aboard *HST* on 1996 January 27 by T. R. Lauer et al. (2000, in preparation). Since they will present the details of the imaging analysis, here we will summarize only the details relevant to NGC 1023. The nucleus was placed in the Planetary Camera, which has a plate scale of 0.″0455 pixel$^{-1}$. Several exposures were obtained through each of the filters F555W and F814W, which are roughly equivalent to the $V$ and $I$ filters. The total signal attained at the nucleus was roughly 22,000 $e^-$ pixel$^{-1}$ and 36,000 $e^-$ pixel$^{-1}$, respectively. The images were reduced and deconvolved with 40 iterations of the Lucy-Richardson method (Lucy 1974; Richardson 1972). We measured the surface photometry in Figure 1 using isophote fits as described in Lauer et al. (1995). We need to find a fit to this surface brightness profile because in § 3.2 we will examine the effects of the STIS point spread function (PSF). First, we fit a Nuker law (Lauer et al. 1995; Faber et al. 1997)

$$I(r) = 2^{(\beta-\gamma)/\alpha} I_b \left(\frac{r_b}{r}\right)^{\gamma} \left[1 + \left(\frac{r}{r_b}\right)^{\alpha}\right]^{(\gamma-\beta)/\alpha}, \qquad (1)$$

where $I_b$ corresponds to a surface brightness of 16.05 mag arcsecond$^{-2}$, $r_b = 1.''64$, $\alpha = 2.14$, $\beta = 1.26$, and $\gamma = 0.70$. This profile is a steep, largely featureless power law, characteristic of the profiles in early-type galaxies with modest bulge luminosity (Faber et al. 1997). The central two points in the profile were excluded from the Nuker law fit, since this law does not apply to such sharp increases in intensity right at the nucleus. Thus, we confirm the detection of the compact nuclear component (presumably a nuclear stellar cluster) in NGC 1023 by Lauer et al. (1995). To fit the nuclear star cluster, we added the following function to the fitted Nuker law

$$I(r) = \frac{I_0}{[1 + (r/r_0)^2]^n}, \qquad (2)$$

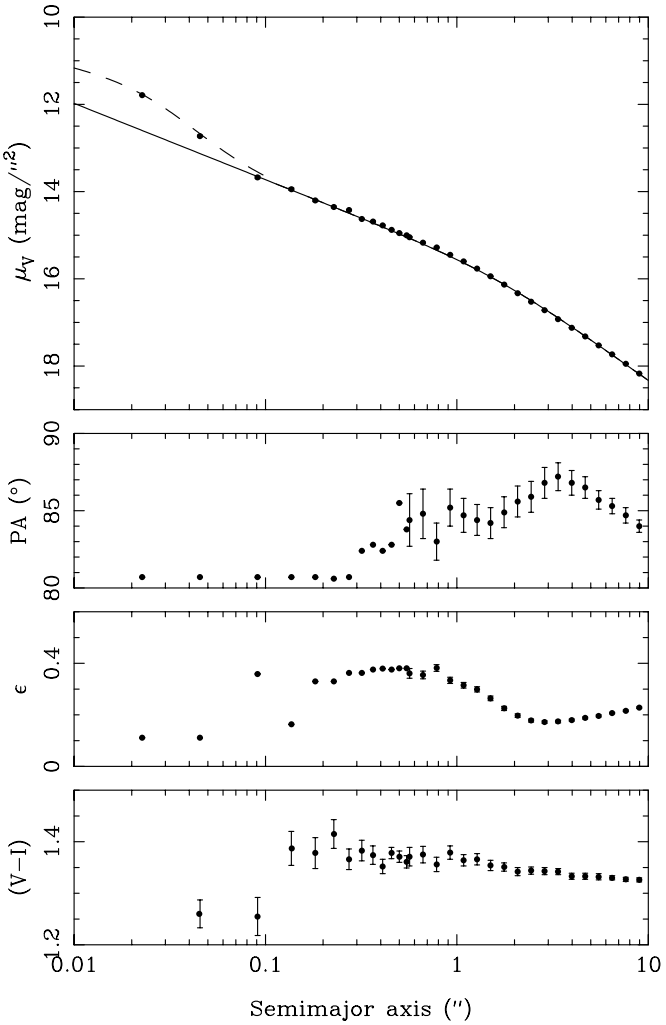


FIG. 1.—Major-axis surface photometry of NGC 1023, including surface brightness $\mu_V$, position angle P.A., ellipticity $\epsilon$, and $(V-I)$. The fits to the surface brightness profile include a Nuker law (*solid line*) and a Nuker law plus model for the nuclear stellar cluster (*dashed line*).

where $I_0 = 11.69$ mag arcsecond$^{-2}$, $r_0 = 0.''035$, and $n = 2.0$. This fit was constrained with the inner three data points in the profile and the total flux in the STIS spectrum (§ 2.2) within 0.″075 of the nucleus [given an adopted $(V-I)$ of 1.4]. The profile of the nuclear cluster cannot be much steeper without violating at least one of these constraints. We use this fit to the observed profile only in § 3.2. In our analysis in § 4 where we construct dynamical models, we use the photometric data instead.

To extend the photometry to larger radius, we added the photographic photometry of NGC 1023 from Barbon & Capaccioli (1975). Their photographic plates show a "cloud" ∼2.″7 east of the nucleus, which is presumably an individual dwarf galaxy perhaps in the process of merging with NGC 1023. Since our kinematic data discussed below extend out to only ∼100″ from the nucleus, our galaxy dynamical models (§ 4) are only applicable inside this radius. Therefore, we ignore this dwarf galaxy by adopting Barbon & Capaccioli's (1975) surface brightness data for the west side of the galaxy (away from the companion dwarf galaxy). We verified Barbon & Capaccioli's (1975) surface photometry by comparing it to the intensity along the slit from the ground-based spectroscopy described in § 2.2 near

5200 Å from K. Gebhardt et al. (2000, in preparation). In order to combine *B*-band photographic surface photometry with the *V*-band *HST* surface photometry, we normalized their photographic data by adopting $(B-V) = 1.0$ (de Vaucouleurs et al. 1991).

### 2.2. *Long-Slit Spectroscopy*

The primary set of ground-based long-slit spectroscopic observations of NGC 1023 will be presented in K. Gebhardt et al. (2000, in preparation). For these observations, their 1″ wide slit was aligned along the three position angles (P.A.) of 0°, 90°, and 45°. The first two angles correspond to the photometric minor and major axes. The spatial resolution (dominated by atmospheric seeing) was ≈1.″0 (FWHM). The spectra covered 4765–5788 Å, which includes the absorption lines of Mg I *b* (5167 Å, 5172 Å, and 5183 Å), with a resolution (FWHM) of 3.1 Å.

Since the measurement of stellar kinematics is usually easier using the Ca II triplet (8498 Å, 8542 Å, and 8662 Å) absorption lines compared to Mg I *b*, we obtained additional long-slit spectra of NGC 1023 with the KPNO 4 m telescope covering the Ca II triplet. Table 1 lists the details of our KPNO observation, including the detector employed, wavelength coverage, slit size, and spectral resolution. We observed at the P.A.s of 0° and 90°. The atmospheric seeing was 1.″8–2.″2 (FWHM). The nucleus was placed in the slit, as viewed through the telescope guide camera, prior to the start of each galaxy exposure. We eliminated the possibility of centering errors caused by differential atmospheric refraction between the guide camera and the spectrograph slit by mounting an *I*-band filter in front of the guide camera. Galaxy exposures were typically 1800 s in duration, after which a spectrum of the comparison lamp was obtained. The spectrum of a nearby faint star was then obtained to measure the seeing-dominated PSF in the spatial direction. The galaxy nucleus was then carefully moved along the slit by ≈5 pixels, and another exposure was taken. We repeated this exposure sequence for 2–4 hours of integration time per slit P.A.; the signal-to-noise ratio (S/N) in the reduced spectra is ≈100 $Å^{-1}$ at the nucleus.

Spectra of bright K giant stars (to serve as template spectra during the analysis) were obtained during twilight.

The spectra were calibrated using standard techniques in IRAF for optical long-slit spectroscopy. Wavelength calibration was established from the positions of several emission lines in the comparison spectra, providing for wavelength calibrations accurate to ±0.08 Å. The continuum peaks in the spatial profile of each galaxy exposure were aligned before combining the individual spectra.

Now we describe our observing procedure using *HST*/STIS. To obtain a stellar template spectrum needed for measuring the stellar kinematics in a galaxy STIS spectrum, the K0 III star HR 7615 was observed with the STIS CCD on 1997 October 23. The instrumental setup was identical to that of the NGC 1023 visit described below. Spectra were obtained with the star at each of five positions along the slit width (i.e., along the dispersion axis), corresponding to −0.″10, −0.″05, 0.″00, +0.″05, and +0.″10 (where the origin is at the slit center). The star was stepped along the slit in this way so that during data analysis we could combine the individual template spectra using the appropriate weights to match the slit illumination profile of a galaxy. Small displacements away from the slit center cause small shifts of the spectrum along the dispersion axis. We must correct for this effect, in order to derive the galaxy dynamics as accurately as possible. For calibration purposes, we also obtained spectra of the internal wavelength calibration source (wavecals) and the internal continuum lamp. This contemporaneous flat field spectrum was obtained (while HR 7615 was occulted by the Earth) through the 0.″3 × 0.″09 (length × width) slit rather than the long slit to simulate the illumination pattern of a point source at the detector plane, because the internal continuum lamp illuminates the slit plane uniformly. The purpose of such contemporaneous flat fields is to provide for proper calibration of the internal fringing that is significant at $\lambda \geq 7500$ Å (see Goudfrooij, Baum, & Walsh 1997).

The STIS CCD observations of NGC 1023 were obtained on 1997 November 13. The slit was aligned at a P.A. of 93° (observing constraints prevented the slit from being aligned more closely with the major axis). Table 1 lists the detailed configuration of STIS during this observation. We integrated for three *HST* orbits at the calcium triplet (using the grating G750M) for a total integration time of 7574 s. Two successive exposures were obtained during each orbit to identify cosmic-ray events, and NGC 1023's nucleus was shifted by 4 pixels along the slit before resuming integration in the next orbit. Wavecals were interspersed among the galaxy exposures to allow for wavelength calibration with correction of thermal drifts during data reduction. Contemporaneous flat fields through the same long slit were obtained while NGC 1023 was occulted by the Earth.

TABLE 1

INSTRUMENTATION DETAILS

| Quantity | KPNO | *HST* |
|---|---|---|
| Spectrograph | RC | STIS |
| Observation dates | 1997 Feb 15–16 | 1997 Nov 13 |
| Detector | Tek 2048 × 2048 | SITe 1024 × 1024 |
| Gain ($e^-$ $ADU^{-1}$) | 1.9 | 1.0 |
| Wavelength coverage (Å) | 7490–9861 | 8272–8845 |
| Reciprocal dispersion (Å $pixel^{-1}$) | 1.14 | 0.56 |
| Slit width (arcsec) | 1 | 0.2 |
| Comparison line FWHM (pixel) | 2.0 | 3.1 |
| $R = \lambda/\Delta\lambda$ | 3800 | 4930 |
| Instrumental dispersion ($\sigma_I$) (km $s^{-1}$) | 60 | 56 |
| Spatial scale (arcsec $pixel^{-1}$) | 0.69 | 0.050 |
| Slit length (arcmin) | 5.5 | 0.8 |

The reduction of STIS spectroscopic data covering the calcium triplet is not straightforward. The reduced data for this STIS mode provided by the STScI pipeline are not optimal. Their technique for rejection of hot pixel events (see Kimble et al. 1998) relies on daily monitoring of the dark image. However, we found that hot pixels stronger than 9 $\sigma$ above the background do not subtract very well, presumably because such hot pixels vary in intensity on timescales of less than 1 day. Also, the STScI pipeline uses a library flat field rather than the contemporaneous flat field obtained during the observations, and their geometric rectification is not sufficient for our purpose. With these limitations noted, we found that the basic reduction steps (bias subtraction, dark subtraction, and combining the subexposures to reject cosmic-ray events) of the CALSTIS task in the STIS package of STSDAS could be made to work, if the dark calibration image employed was first median filtered to reject hot pixels greater than 9 $\sigma$ above the background. These strong hot pixels were cleaned out later (see below). For the remainder of the reduction, we utilized standard procedures in IRAF for long-slit spectroscopy. For each science spectrum, we constructed a fringe flat from its associated contemporaneous flat field, using a third-order polynomial to normalize the flat field and remove the color of the lamp. We tested the alignment of the fringe pattern between the contemporaneous flat-field images and the data by shifting the phase and amplitudes of the contemporaneous fringe flats by arbitrary factors and then dividing these into the data. Based on the residuals seen in the continuum (compared to our KPNO spectra), we found that the original unshifted and unscaled fringe flats were the best flat field for the data. The remaining hot pixels were then cleaned out of each image in the following way. We divided each image by a heavily median filtered version of itself, to emphasize hot pixels near the galaxy nucleus where the intensity profile along the slit is steep. The resulting images were then cleaned of hot pixels using a local median filter that replaced any pixels deviant from its neighbors by more than 3 $\sigma$ with the median value of its neighbors. Neighboring pixels were defined either by a $5 \times 1$ pixel box near the galaxy center with the long dimension in the dispersion direction or by a $5 \times 5$ box away from the galaxy center. These cleaned images were then multiplied by the original median filtered image to restore the intensity profile along the slit. We tested this cleaning process extensively to ensure that the data were not significantly compromised. Wavelength solutions and corrections for the geometric distortions were determined from the wavecals and traces of the position of the continuum peak across the CCD. Although the position of the continuum peak near the central row of the CCD varies at a uniform rate as a function of CCD column number, the geometric distortion is not a simple rotation because the positions of the emission lines in the wavecals do not vary at a uniform rate as a function of CCD row number. The data were then resampled only once to register the galaxy center to the same row in each image and to bin the dispersion axis on a log $\lambda$ scale. After this geometric correction had been applied, the rms residual about a perfect correction was 0.05 pixel and demonstrated no systematic behavior with CCD pixel coordinates. We combined the individual galaxy exposures by taking the average (weighted by exposure time). Finally, we applied STScI's pipeline sensitivity curve to flux-calibrate the data, since this sensitivity curve has a low-order structure that, if not removed, would adversely affect our ability to measure the wings of very broad galaxy absorption-line profiles. The HR 7615 spectra have at least 44,000 $e^-$ pixel$^{-1}$ (depending on the star's position with respect to the slit center). Since our flat-field image has only $\approx$11,000 $e^-$ pixel$^{-1}$, the S/N in the HR 7615 spectra is limited to 150 Å$^{-1}$. For NGC 1023, the S/N is 40 Å$^{-1}$ in the row centered on the nucleus. As mentioned above, we combined the individual spectra of HR 7615 to match the slit illumination pattern of NGC 1023 along the dispersion axis.

## 3. MEASUREMENT OF THE STELLAR KINEMATICS

In this section, we briefly review the method we utilized to measure the stellar kinematics from the spectra. Next we examine possible effects of the STIS/CCD PSF on the stellar kinematics, and then verify that those effects are represented adequately during construction of galaxy dynamical models in § 4.

### 3.1. *The Fourier Correlation Quotient Method*

Using the Fourier correlation quotient (FCQ) method (Bender 1990) on the ground-based and STIS spectra, we measure the line-of-sight velocity distribution (LOSVD) $f(v)$ for each extracted spectrum along the slit (where the extracted apertures were defined to match the binning scheme of the three-integral models discussed in § 4.2). Those models require as input the nonparametric LOSVD as a function of position in the galaxy. FCQ also determines the moments of the LOSVD which are needed for the two-integral models constructed in § 4.1. These moments are determined by fitting the LOSVD with a Gaussian (with radial velocity $V$ and velocity dispersion $\sigma$) plus third- and fourth-order Gauss-Hermite polynomials $H_3$ and $H_4$ (van der Marel & Franx 1993; Gerhard 1993; Bender, Saglia, & Gerhard 1994), i.e.,

$$f(v) = \frac{\gamma}{\sqrt{2\pi}\sigma} e^{-(v-V)^2/2\sigma^2} \times \left[1 + h_3 H_3\left(\frac{v-V}{\sigma}\right) + h_4 H_4\left(\frac{v-V}{\sigma}\right)\right], \quad (3)$$

where $\gamma$ is the strength of the galaxy absorption line relative to that of the template star. The coefficients $h_3$ and $h_4$, respectively, quantify the lowest order asymmetric and symmetric deviations of the LOSVD from a Gaussian. If $h_3 > 0$, then the blue side of the line profile is steeper than the red side, while the opposite is the case if $h_3 < 0$. If $h_4 > 0$, then the line profile is more triangular than a Gaussian, i.e., it is more strongly peaked and has wings that are more extended. If $h_4 < 0$, then the line profile is more rectangular than a Gaussian, i.e., it has a flatter top and less extended wings. Nonzero values of $h_3$ can arise when the galaxy has two or more velocity components, or if the radial rotation gradient is steep such that both low and high velocities are seen in projection along the line of sight. Nonzero values of $h_4$ indicate that the galaxy's velocity distribution function is anisotropic. Figure 2 shows the FCQ results for the nuclear row of the STIS spectrum of NGC 1023. We determine the errors in the LOSVDs by Monte Carlo simulation. This involves convolving the template spectrum with the FCQ estimate of the LOSVD and (given the S/N in an extracted galaxy spectrum) finding 30 different noise realizations of a synthetic galaxy spectrum. For simplicity, we assume that

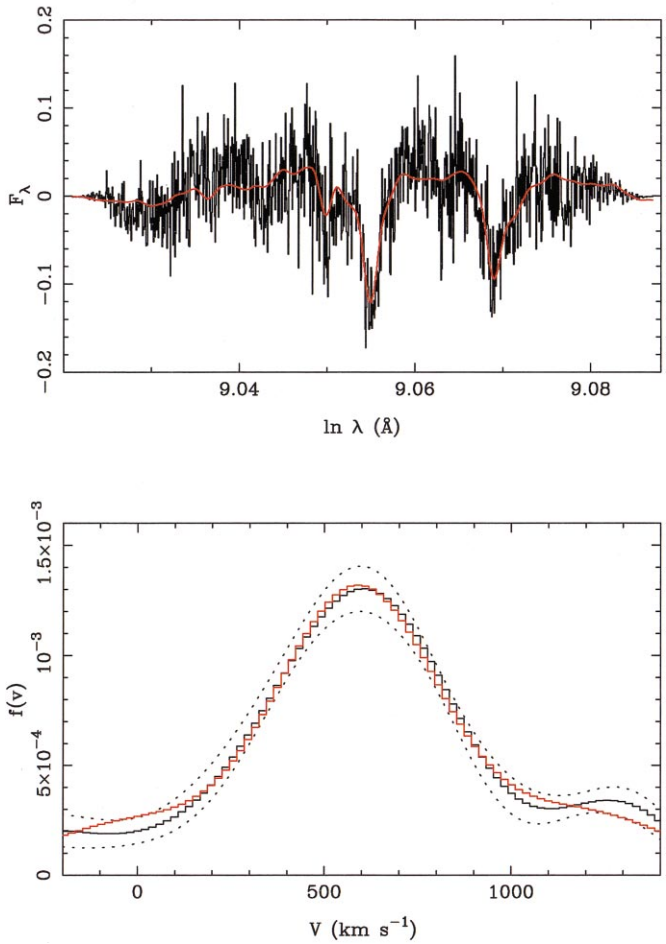


FIG. 2.—Results from the FCQ method for the nuclear row of the STIS spectrum of NGC 1023. The top panel shows the galaxy spectrum (*black*) and the template spectrum (*red*) after it has been convolved with the parametric LOSVD for this row. Both spectra have been continuum subtracted and have been tapered at the ends using a cosine bell. The lower panel shows the nonparametric (*black*) and parametric (*red*) LOSVDs. The dashed curves represent the 68% confidence interval for the nonparametric LOSVD. The Gauss-Hermite moments for this fit are $V = 595 \pm 18$ km s$^{-1}$, $\sigma = 295 \pm 30$ km s$^{-1}$, $h_3 = -0.021 \pm 0.056$, and $h_4 = 0.162 \pm 0.056$.

the noise distribution in amplitude is Gaussian, which is nearly identical to a Poisson distribution for these high count levels. The synthetic galaxy and template spectra are then input into FCQ, providing a sample of the error distribution in the LOSVD.

Figure 3 shows the Gauss-Hermite moments measured from the STIS and ground-based spectra as a function of distance from the nucleus. A preliminary examination of these data show that $\sigma$ increases significantly toward the nucleus (where $\sigma = 295 \pm 30$ km s$^{-1}$), which could indicate the presence of a nuclear BH. In § 4, the data in Figure 3 will be compared to dynamical models. In the meantime, next we examine the effects of the STIS/CCD PSF on the data.

### 3.2. *Effects of the STIS/CCD PSF*

During our initial application of FCQ to the STIS spectrum of NGC 1023, we became aware that the STIS PSF might be asymmetric at ~8500 Å. Given this galaxy's steep power-law surface brightness profile (Fig. 1), we were concerned that the off-nuclear spectra might be distorted by the nuclear spectrum in a way that is asymmetric along the slit. During the construction of galaxy dynamical models (§ 4), we convolve the dynamical models with a modeled PSF before comparison with the observations. This step is intended to correct for the effects of the PSF, but this model PSF must be circularly symmetric. It would not be straightforward at all to allow for an asymmetric PSF when constructing dynamical models. Besides, we can measure the STIS PSF at this wavelength only along the slit (which we describe below), so we have no knowledge about its two-dimensional structure. (Although STIS has an imaging mode, there are no filters with sufficiently narrow bandpass in the near-infrared to isolate the PSF asymmetry which is caused by diffraction effects.)

We measure the STIS PSF from the spectrum of the template star HR 7615. The main complication is that at ~8500 Å, the FWHM of the PSF is approximately 1.5 pixels, so the PSF is undersampled. Consequently, a simple cut along the spatial axis of a point-source spectrum does not provide an adequate description of the PSF because the profile is adversely affected by aliasing. One way to recover an oversampled measurement of the PSF from such data would be to dither a point source along the slit by fractional pixels between exposures. To find the PSF, the profiles along the slit would then be combined by interleaving the pixels.

Even though during our observation HR 7615 was not dithered along the spatial axis of the slit by moving the telescope, the geometric distortions in the STIS/CCD camera are such that the position of the stellar peak varies slowly as a function of distance along the dispersion axis in the raw data. The amplitude of this geometric distortion is ≈6 rows across the 1024 columns along the dispersion axis. The rate that the position of the stellar peak changes per CCD column is approximately constant as a function of CCD column number (see § 2), so the spatial profile of the source is effectively dithered along the slit by ≈0.006 pixels per column. Using this effect to our advantage, we reconstruct an oversampled measurement of the PSF using the spectrum of HR 7615 with the star centered in the slit. For the present purpose, the input spectrum is from an intermediate step during data reduction (just prior to geometric correction). The PSF is determined as a function of position along the dispersion axis in spectral bins 9 columns wide. Such binning is necessary to obtain a PSF with very high S/N for accurate centering. The relative geometric distortion across a 9 pixel bin is ~0.054 pixels, which is negligible compared to the PSF FWHM (≈1.5 pixels). The PSF from each of the bins is prepared to be interleaved with the PSF from the other bins by normalizing each by the total flux (within a distance of 10 pixels of the peak) along the slit and shifting the pixel coordinates so that the centroid of the PSF in each bin is identical. The pixel intensity values are not altered in any way during this process. We also measured the PSF from the spectrum of the K3 III star HR 260 obtained by G. A. Bower et al. (2000, in preparation) on 1998 March 15, using the same instrumental setup as our HR 7615 visit. These reconstructed PSFs are shown in Figure 4. The PSFs derived from separate stars agree extremely well: there was no variation in the PSF at this epoch on a timescale of 5 months.

The PSF in Figure 4 has FWHM = 1.58 pixels (0.″079) and has broad asymmetric wings, which peak at $R = \pm 2$ pixels. These wings represent the first Airy ring in the PSF and are asymmetric probably because the two-element corrector optics in STIS might not be perfectly aligned for this

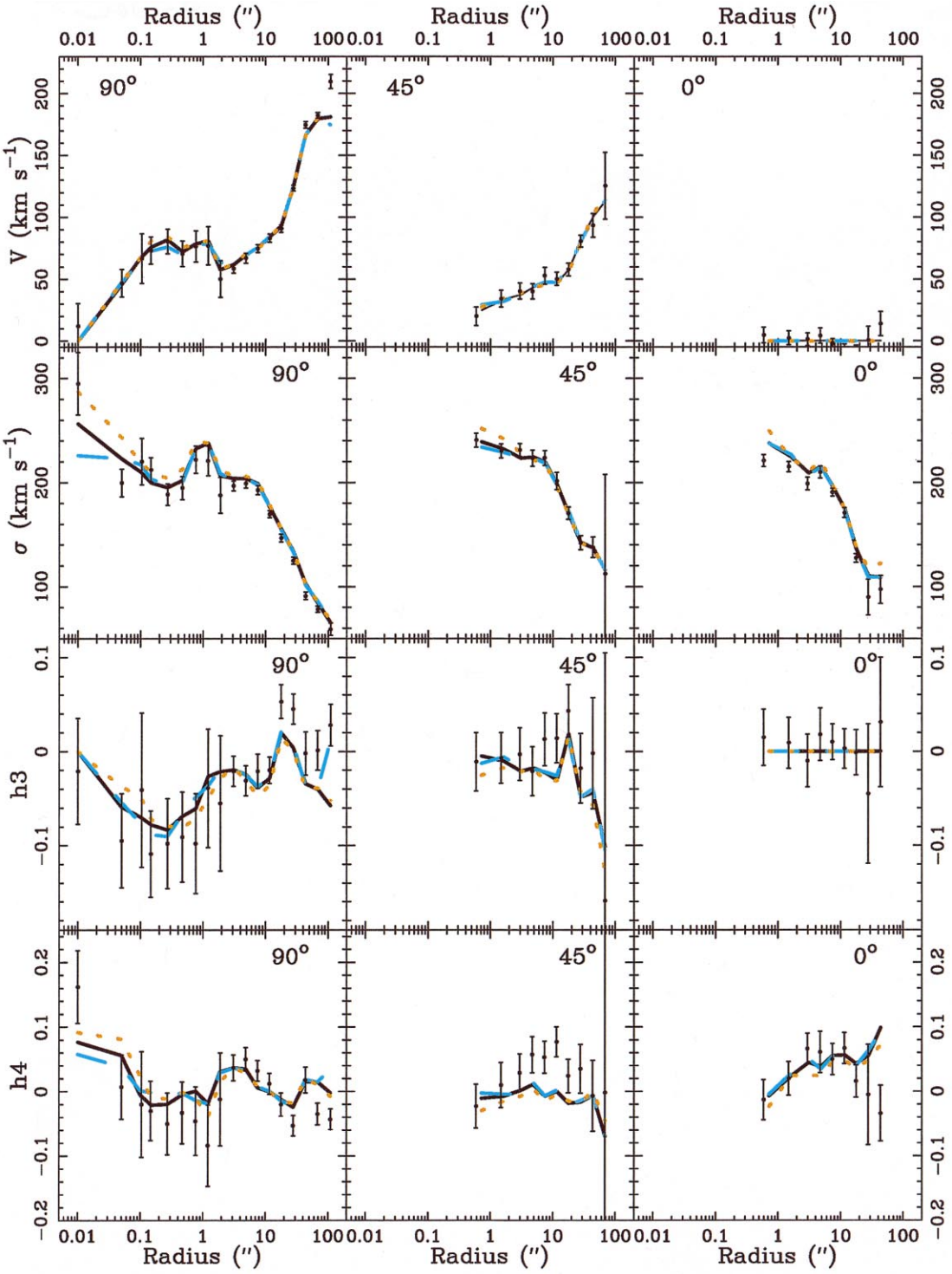


FIG. 3.—Gauss-Hermite moments measured from the STIS and ground-based spectra utilizing the Fourier correlation quotient method. Each column of panels shows the four Gauss-Hermite moments for a given slit position angle that we observed. The curves show three of the edge-on axisymmetric models that we construct in § 4.2. All three have $M/L_V = 5.6$ and include the best-fitting BH of $5.6 \times 10^7\ M_\odot$ (*solid line*), no BH (*dashed blue*), and a BH of $2.2 \times 10^8\ M_\odot$ (*dotted brown*).

wavelength (C. W. Bowers, private communication). The purpose of these corrector optics is to correct for the *HST* primary mirror's spherical aberration and for the astigmatism at the STIS field of view in *HST*'s aperture plane (Kimble et al. 1998; Woodgate et al. 1998).

Could the asymmetric wings on the PSF significantly distort our measurements of the stellar kinematics? To test this possibility, we construct a simulated spectrum of NGC 1023 from the spectrum of HR 7615 using the empirical fit to NGC 1023's surface brightness profile $\mu_V(R)$ (*dashed line* in Fig. 1) and a simple empirical model of the stellar kinematics. In this model, $V(r)$ and $\sigma(r)$ are set to simple analytical forms [representative of the $V(r)$ and $\sigma(r)$ profiles determined from the observed galaxy spectrum] and $h_3$ and $h_4$ are set to zero at all radii. This model galaxy spectrum is then input into a STIS simulator that (1) applies

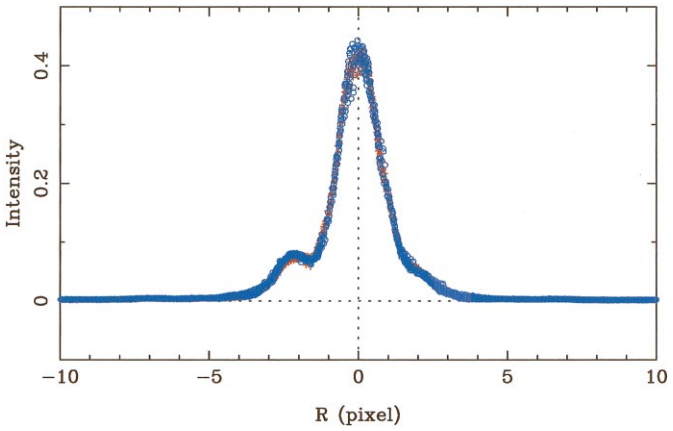


FIG. 4.—Reconstructed STIS/CCD PSFs using the spectra of the template stars HR 7615 (*blue points*) and HR 260 (*red points*). The agreement between the two PSF measurements is so good that the two are almost indistinguishable. The sign convention on the abscissa is defined such that increasing $R$ corresponds to increasing row number along the spatial axis on the CCD.

the spectrograph's sensitivity curve and the integration time to convert from flux units to detector counts, (2) convolves the spectrum with an input PSF, and (3) adds Gaussian noise to simulate the S/N in the real observation. For each simulation, four spectra are saved to cover all possibilities with steps 2 and 3 independently turned on or off. We generate two sets of simulated spectra: one for the observed PSF from Figure 4, and one for the model PSF used during modeling in § 4. This model PSF was constructed from the observed PSF by folding it about $R = 0$ and then determining the average within radial bins of 0.1 pixel. The purpose of these simulations is to examine the effects of the observed PSF and to check that the model PSF faithfully reproduces any such effects within the errors.

We then input all simulated spectra into FCQ to examine the effects of the PSF and noise, yielding the results in Figure 5. Panel *a* of Figure 5 shows that the most significant effect of the PSF is to smear out the $\sigma$ profile, as expected. The most important result, however, is seen in panel *b* of Figure 5. The kinematic measurements from the simulated spectra using the observed PSF or our model PSF are not statistically different, even when noise is not added to the spectrum. This demonstrates that the model PSF reproduces the effects of the observed PSF and justifies our approximation that the PSF is symmetric.

## 4. DYNAMICAL MODELING

In this section, we construct galaxy dynamical models from the observed surface photometry and stellar kinematics, to determine if the observations require the presence of a dark compact object. We utilize the independent modeling algorithms of Magorrian et al. (1998) and Gebhardt et al. (2000b). Both of these references should be consulted for a general discussion of these techniques. In this paper we provide only a brief summary and the details of the models constructed for NGC 1023. Both algorithms assume that

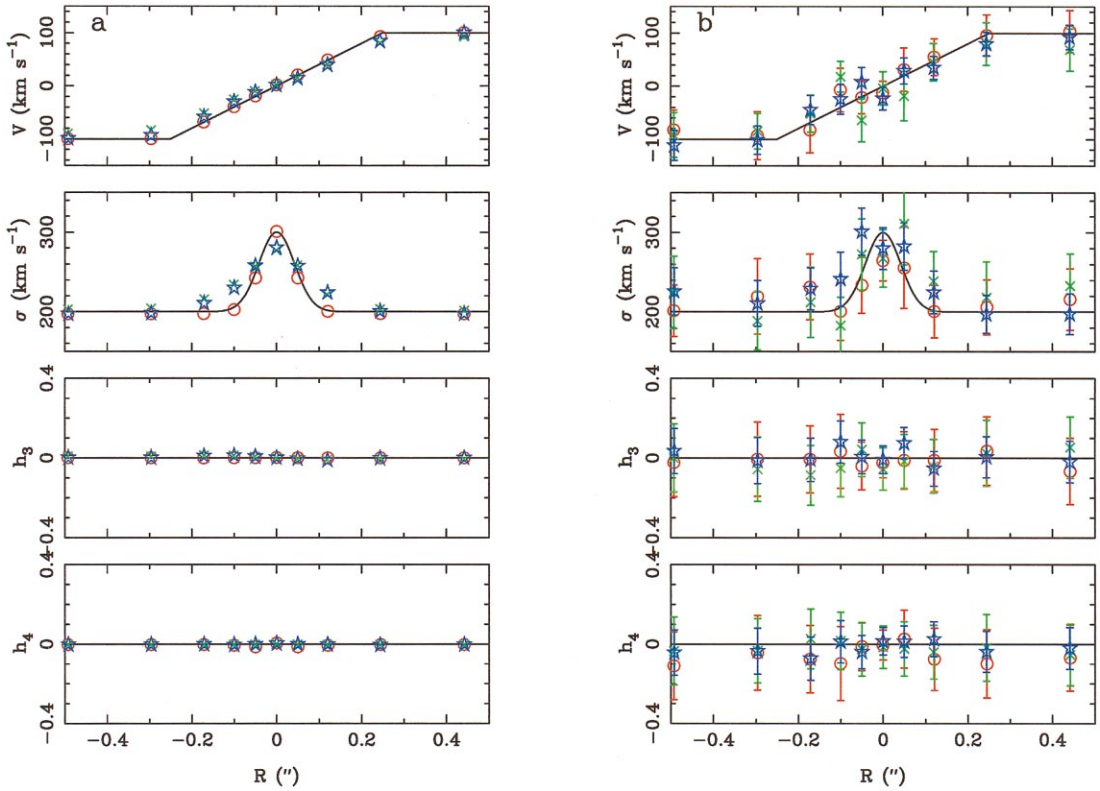


FIG. 5.—Stellar kinematics measured from simulated STIS spectra of NGC 1023 to investigate possible effects of the asymmetric PSF. Solid lines represent the simple empirical kinematical model from which the simulated spectra were constructed. (*a*) Simulations without noise added to the spectra. (*b*) Simulations that include noise. The red open circles show the measurements from the simulated spectrum before convolution with the PSF, and the green crosses and blue stars represent, respectively, the measurements from the spectrum convolved with the PSF from Fig. 4 (i.e., the actual PSF) or the model PSF (see text). The error bars in (*a*) are no larger than the size of the points. The most important result is that the green crosses and blue stars agree, which justifies our approximation in § 4 that the PSF is symmetric.

the galaxy mass distribution is axisymmetric with constant inclination ($i$, with respect to the plane of the sky). That assumption is justified by the behavior of P.A. and ellipticity as a function of radius at $R < 10''$ (Fig. 1), which are nearly constant with radius at values of 83° and 0.28, respectively. A nonaxisymmetric density distribution (such as a triaxial one) should exhibit significant radial variations in one or both of these quantities. The two modeling algorithms differ dramatically in the way that the internal dynamics are modeled. Magorrian et al.'s (1998) algorithm assumes that the velocity distribution function is a function of only the orbital energy $E$ and angular momentum $L_z$ about the polar axis with an isotropic velocity dispersion tensor. It then solves the Jeans equations to construct a model. This process is straightforward for a given galaxy. Gebhardt et al.'s (2000b) algorithm assumes three integrals of motion, $E$, $L_z$, and $I_3$ (see Binney & Tremaine 1987). It utilizes Schwarzschild's (1979) orbit-based method constrained by Richstone & Tremaine's (1988) maximum entropy technique. Consequently, the three-integral models are more computationally intensive to construct but allow for a fully general axisymmetric model. This section is subdivided to discuss the results of each modeling algorithm when applied to NGC 1023.

### 4.1. *Two-Integral Models*

Magorrian et al.'s (1998) method has four steps, which stated briefly are (1) assuming a value $i$, identify a smooth luminosity density $\nu(R, z)$ that projects to an acceptable fit of the observed surface brightness profile $\mu(R)$; (2) calcuate the gravitational potential using assumed values for the mass-to-light ratio ($M/L$) and nuclear black hole mass ($M_{\rm BH}$); (3) solve the Jeans equations for the second-order moments ($\nu\overline{v_\phi^2}$ and $\nu\overline{v_R^2} \equiv \nu\overline{v_z^2}$) of the distribution function; and (4) project the luminosity-weighted zero- and second-order moments of the line-of-sight velocity onto the sky, convolve with the instrumental PSF, and average over the same bins as in the observations. Thus, the free parameters for any model for our observations are $i$, $M/L$, and $M_{\rm BH}$.

The PSF is an important ingredient in the modeling. Since we have kinematic observations from *HST* and the ground and the PSFs are very different, we apply the appropriate PSF to model the different data points. However, we do not model more than one observation at a given position in the galaxy, so we use STIS data within 4″ of the nucleus along the major axis and ground-based data at all other positions. The PSF for ground-based observations is assumed to be Gaussian with the appropriate FWHM as described in § 2. For the STIS data, the model PSF described in § 3.2 is adopted.

Our galaxy models assume that the inclination is constant within the galaxy. Since NGC 1023 is classified as an SB0, we are assuming that the inclination of the bulge and disk are identical. The ellipticity at radii beyond the effective radius of the bulge ($R_e = 36''$; Barbon & Capaccioli 1975) is $\approx 0.60$ and provides a constraint on the inclination. If the vertical thickness of the outer stellar disk is negligible, then the disk would have $i = 66°$. This is a lower limit on the true inclination, because the thickness of the outer disk actually might not be negligible. Consequently, we will construct models only with $i \geq 66°$. Figure 6 shows the kinematics [i.e., the second-order moment $\mu = (V^2 + \sigma^2)^{1/2}$ as a function of radius] of the best-fitting two-integral models for the major and minor axes for $i = 90°$ and $i = 66°$. We do not include the observational data along the intermediate axis in these model fits because doing so caused poor model fits for all three axes. This motivates our construction of three-integral models in § 4.2. For evaluating the goodness of fit of the two-integral models, the figure of merit is $\chi^2 = \sum [(\mu_i - \hat{\mu}_i)^2/\sigma_i^2]$, where $\mu$ and $\hat{\mu}$ are the observed and modeled second-order moments, and $\sigma_i$ is the error in $\mu_i$ describing the 68% confidence band. We find that $\chi^2$ is

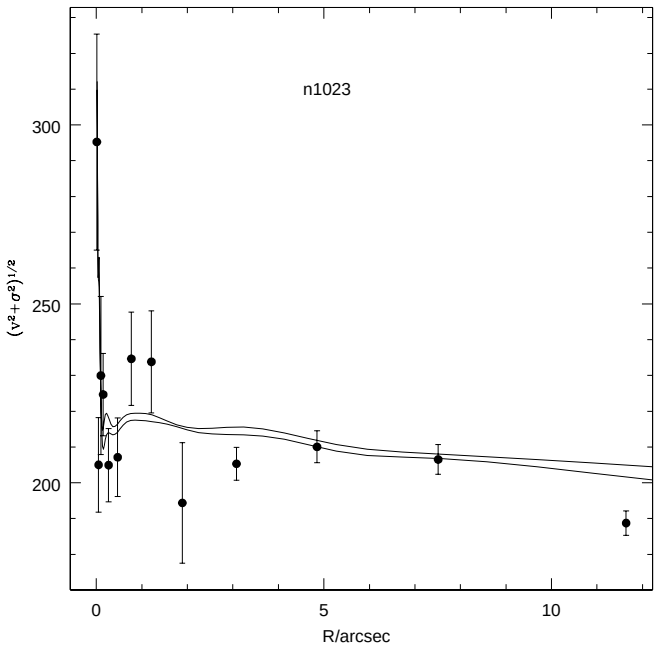


*Fig. 6a*

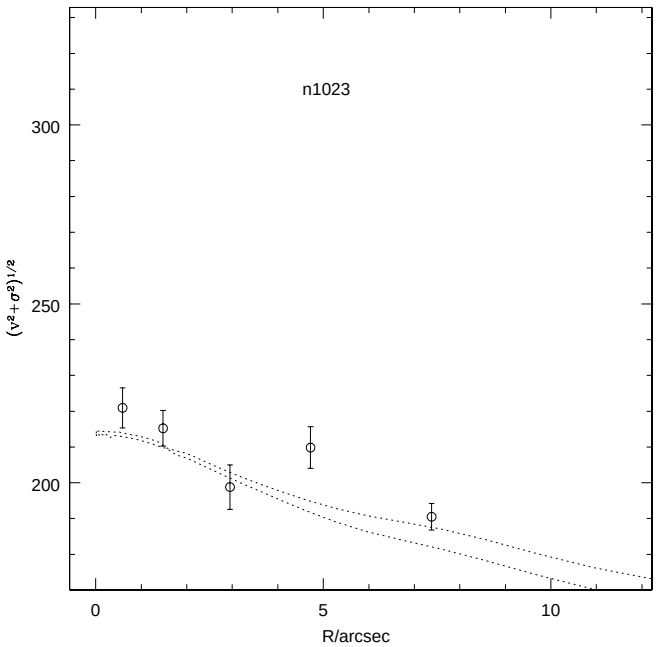


*Fig. 6b*

FIG. 6.—Kinematic profiles of the best-fitting two-integral models along the (*a*) major and (*b*) minor axes of NGC 1023. The plots show the second moment $(V^2 + \sigma^2)^{1/2}$ (in units of km s$^{-1}$) vs. distance $R$ from the center of the galaxy. The points are the observational data. The curves show the best-fitting models for $i = 90°$ and $i = 66°$. The latter model lies above the former.

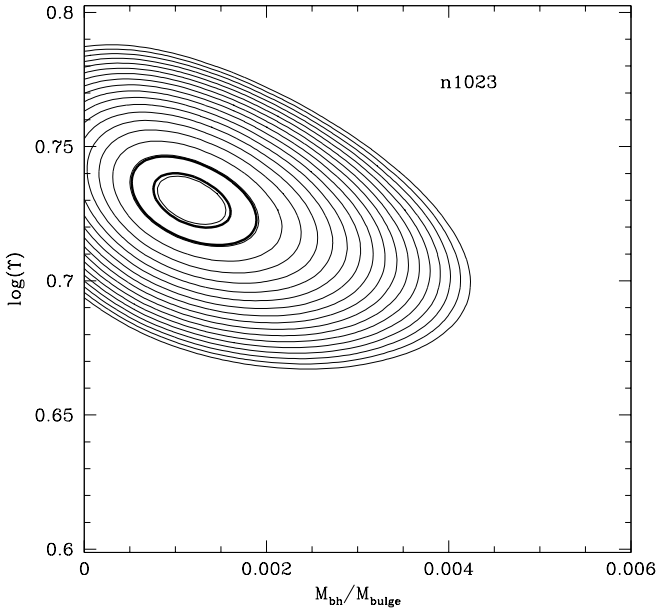


FIG. 7.—Posterior distribution Pr ($\Upsilon$, $M_{BH}|D$) for the two-integral models of NGC 1023 (note that $\Upsilon \equiv M/L_V$). Successive light contours indicate a factor of 10 change in Pr ($\Upsilon$, $M_{BH}|D$). The heavy contours enclose the 68% and 95% confidence regions on $M/L_V$ and $M_{BH}$.

insensitive to reasonable values of $i$ (see above), so we average the best-fitting parameter values over this range in $i$. This yields $M_{BH} = (6.0 \pm 1.4) \times 10^7\ M_\odot$ [which corresponds to $M_{BH}/M_{bulge} = (1.1 \pm 0.2) \times 10^{-3}$], and $M/L_V = 5.38 \pm 0.08$. Figure 7 shows the posterior distribution Pr ($M/L_V$, $M_{BH}|D$) which is the likelihood based on $\chi^2$ of certain values of $M/L_V (\equiv \Upsilon)$ and $M_{BH}$ given the photometric and kinematic data $D$. See Magorrian et al. (1998) for a detailed definition of Pr . These model results provide a useful estimate of the area of parameter space that we will explore more intensively with the three-integral models.

### 4.2. *Three-Integral Models*

Gebhardt et al.'s (2000b) method has three steps, which stated briefly are (1) assuming a value for $i$ and that the mass distribution's ellipticity is constant with radius, deproject the observed surface brightness profile (as in Gebhardt et al. 1996) to estimate the luminosity density (see Fig. 8); (2) working in units of $M/L$ to minimize the computation time required, combine the luminosity density profile with an assumed value for central black hole mass $M_{BH}$ to determine the library of representative stellar orbits that would be possible in that gravitational potential; and (3) for an adopted value of $M/L$, superimpose the orbits from the library (under constraint by maximum entropy) to fit the observed LOSVD as a function of position in the galaxy. These three steps are repeated as necessary to vary $i$, $M/L$, and $M_{BH}$.

The models are binned spatially (as projected onto the sky) and in velocity space (since we are modeling the LOSVD nonparametrically). The spatial bins are in radius $r$ (from the galaxy center) and $\theta$ (the polar angle measured from the major axis). During step 2, we use 80 radial bins, 20 angular bins, and 15 velocity bins, which are approximately logarithmic in $r$, linear in sin $\theta$, and linear in velocity. The bins in $r$ and $\theta$ cover 0.″0025–317″, and 0°–90°, respectively. At small radius where the bins converge, some bins are combined with neighboring bins as needed to mimic the STIS slit width. The bins in velocity are defined in units of $\sqrt{M/L}$ (in solar units) and cover $-337$ to $+337$. The coverage and size of the velocity bins are chosen to include the wings of the LOSVD for the maximum velocity dispersion observed, and to match approximately the instrumental

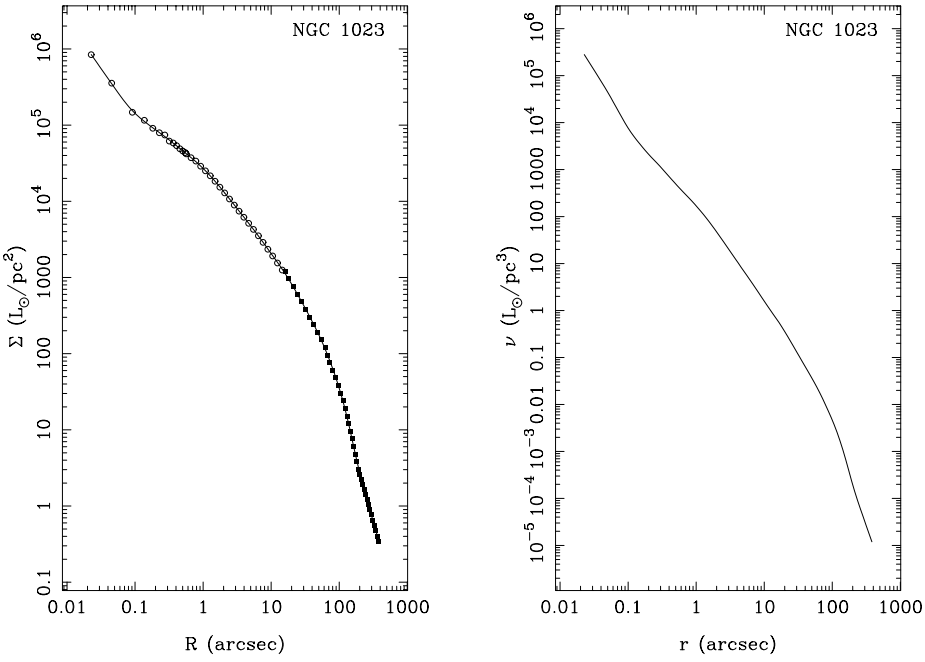


FIG. 8.—Radial profiles of surface brightness and luminosity density in $V$ for NGC 1023 (corrected for Galactic extinction). *Left*: Open circles represent the *HST* data from Fig. 1, while closed squares represent the data from Barbon & Capaccioli (1975) and the extrapolation beyond their last data point at $R = 189''$ using an $R^{1/4}$ law with $R_e = 36''$. The solid line represents a smoothing spline fit to the data. *Right*: The inferred luminosity density for an inclination of 90°. The deprojected density distributions for $i = 80°$ and 70° (for which we will also construct dynamical models) are not shown because their difference from the $i = 90°$ case (1% and 6%, respectively) is insignificant on this scale.

resolution. During step 2, we follow ~3300 orbits per orbital direction (i.e., prograde and retrograde), for a total of ~6600 orbits. During step 3 when comparing the model to the data, the $r$ and $\theta$ bins are compressed from (80 × 20) to (20 × 5) for computational expediency.

The effect of the instrumental PSF is incorporated during step 3. As discussed in § 4.1, we use different PSFs for the *HST* and ground-based data as appropriate, and we fit only the STIS data at radius less than 4″ along the major axis and only the ground-based data at other positions for each of the three P.A.s we observed.

The advantage of our model setup is that almost all model bins correspond exactly to an observational bin, so comparing the model to the data requires almost no interpolation of the model. During the model construction, we match the light in the spatial bins defined above and fit the LOSVDs in the 37 extracted aperture positions where we have data. Therefore, the maximum number of observables is 555 (i.e., 37 positions times 15 velocity bins). However, the actual number of independent observables is smaller than this because FCQ derives the LOSVD with the assistance of an optimal filter in Fourier space (see Bender 1990), whose effect depends on the significance of noise across the cross-correlation function (CCF) between galaxy and template spectra. The filter is more significant for the wings of the CCF where it is noisier relative to the peak. Calculating the actual number of observables would be complicated. Instead, we assume that half of the velocity bins in the LOSVD (i.e., those near the peak) are uncorrelated and the other half are correlated with their adjacent bins. Under that assumption, the number of independent observables would be ~340. Our relative figure of merit is $\chi^2 = \sum [(y_i - Y_i)^2/\sigma_i^2]$, which is the sum over all 555 observables of the deviation between the observational data points $y_i$ and their model fits $Y_i$ given the observational errors $\sigma_i$. Figure 9 shows two example LOSVD model fits to the nuclear LOSVD for models with $M_{\rm BH} = 5.6 \times 10^7\ M_\odot$ and zero (which are discussed below). Since the actual number of degrees of freedom cannot be determined very well, we do not attempt to determine the goodness of fit for a given model from its value of $\chi^2$. Instead, we follow the change in $\chi^2$ as a function of the three model variables ($M_{\rm BH}$, $i$, and $M/L$) and for each model calculate $\Delta\chi^2$ with respect to the minimum $\chi^2$ given by the best-fitting model.

For the best model, the total $\chi^2$ is 274. If the number of degrees of freedom is 340, then the reduced $\chi^2$ would be ~0.8. If the reduced $\chi^2$ should be unity, then we have overestimated either the number of degrees of freedom or the error bars on the LOSVDs. Since this small offset in reduced $\chi^2$ is within our uncertainty of the estimated number of degrees of freedom, we conservatively accept $\Delta\chi^2 = 1$ to define the 68% confidence interval in parameter space.

Our strategy for covering parameter space is to first run models for a low-resolution grid that covers $M_{\rm BH}$ from zero to $2 \times 10^8\ M_\odot$, $i$ of 90°–70°, and $M/L_V$ of 5.0–7.4 in solar units. Based on that grid, we find a preliminary estimate for the location of the $\chi^2$ minimum. Then we run models for a higher resolution grid concentrated around the apparent minimum. Although the two-integral models in § 4.1 are insensitive to the value of $i$, the three-integral models are very sensitive to $i$. The best-fitting models have $i = 90°$. In fact, for models with $i \le 80°$, $\chi^2$ increases to at least 400. Since the fits of the edge-on models are vastly superior, we will not discuss the $i \neq 90°$ models in detail any further. However, the most likely reason for this difference is our exclusion of a dark halo, since that limits our ability to model successfully the kinematics at large radii. To find the confidence band in parameter space, very good coverage in parameter space is beneficial. However, the models are computationally intensive. Since the surface of $\chi^2$ is relatively smooth, we utilize a bicubic spline interpolation of the values of $\chi^2(M_{\rm BH}, M/L_V)$ to estimate the value of $\chi^2$ where we do not have models. Figure 10 shows these contours of $\Delta\chi^2$ superimposed on a grid showing the positions in parameter space of the useful edge-on models. The best model has $M_{\rm BH} = 4.2 \times 10^7\ M_\odot$ and $M/L_V = 5.57$. Figure 11 shows $\chi^2(M_{\rm BH} | M/L_V = 5.6)$, a one-dimensional projection of $\chi^2$ near the minimum. Figure 11 indicates that $\chi^2$ near the minimum changes slowly as a function of BH mass, since it is constrained only by the central few LOSVD measurements. The models are very sensitive to $M/L_V$ because the total mass is well constrained. The three-integral models fit the entire LOSVD at each point along the slit, whereas the two-integral models fit only the profile of the second moment. Given the model assumptions, the range of values in the formal 68% confidence region is $M_{\rm BH}$ of $(3.5 \times 10^7)$–$(4.3 \times 10^7)\ M_\odot$ and $M/L_V$ of 5.54–5.58.

The three-integral models fit the observed LOSVD at each observed position in the galaxy, yet we also determine the model Gauss-Hermite moments by fitting equation (2)

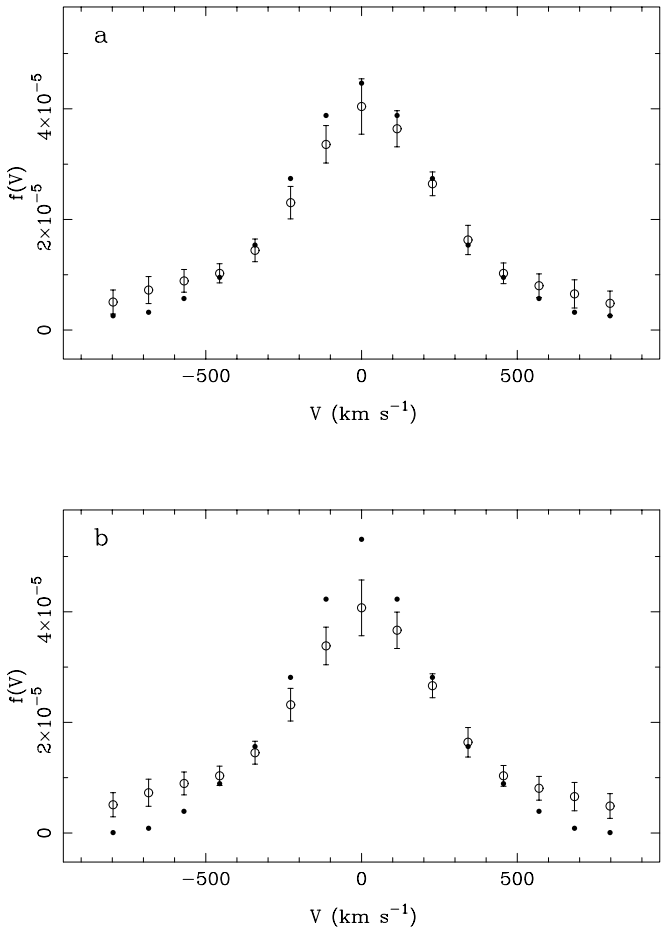


FIG. 9.—Projected LOSVD at the nucleus (*open circles*) and the model fits to it (*solid points*) for the (*a*) $M_{\rm BH} = 5.6 \times 10^7\ M_\odot$ model and (*b*) no BH model.

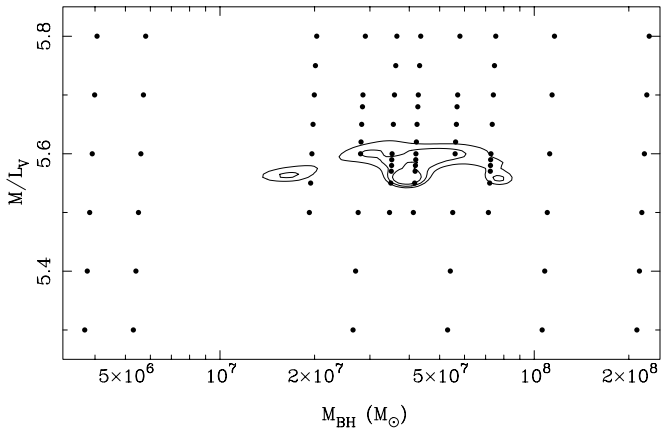


FIG. 10.—Contours of $\Delta\chi^2$ (with values of 1.0, 3.84, and 6.63). One-dimensional projections of these contours correspond to the confidence bands of 68%, 95%, and 99%, on the black hole mass and mass-to-light ratio. The solid points show the positions in parameter space of the models near the $\chi^2$ minimum.

to the model LOSVDs. This provides for a comparison between the observations and models where the effects of a BH are more straightforward to visualize (relative to comparisons between the observed and model LOSVDs, e.g., Fig. 9). In Figure 3, we show the Gauss-Hermite moments for three of the models (including a model near the best fit, and models without a BH and where the BH is much too massive), superimposed on the data. Although this comparison in Figure 3 is instructive, this is not the optimal way of comparing models to the data, since $\chi^2$ is determined by the fit to the LOSVD, not to its moments. Also, since we do not include a dark halo component, we cannot expect to fit the kinematic data at radii $\gtrsim 100''$ (5 kpc). Nevertheless, it is now straightforward to see the reason that models without a BH fail. Along the major axis, the rotation is rapid ($V \approx 70$ km s$^{-1}$ at $R = 0''.1$), while $\sigma$ is increasing toward the nucleus. For models without a BH, fitting the rapid rotation requires populating more tangential orbits, yet overpopulating a single class of orbits restrains $\sigma$ from increasing toward the nucleus. Alternatively, the model with $M_{\rm BH} = 2.2 \times 10^8\ M_\odot$ yields a $\sigma$ profile that is too steep toward the nucleus. The model with $M_{\rm BH} = 5.6 \times 10^7\ M_\odot$ achieves a compromise between these two extremes.

To summarize this section, we have constructed both two-integral and three-integral axisymmetric dynamical models. Both methods point strongly to the presence of a nuclear dark compact object (which presumably is a supermassive black hole). The best-fitting values of BH mass and $M/L_V$ from the two methods are not quite in formal agreement. The BH and $M/L_V$ results from the two-integral models differ from those from the three-integral models by 53% and 3%, respectively.

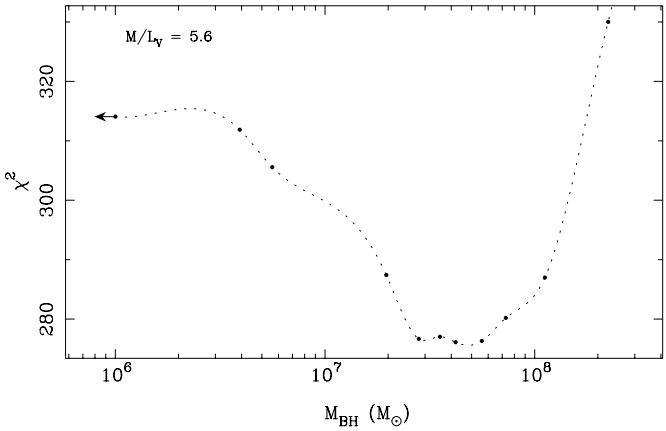


FIG. 11.—One-dimensional projection of $\chi^2(M_{\rm BH}, M/L_V)$ onto the axis of $M_{\rm BH}$ for $M/L_V = 5.6$. The points represent the models, and the dashed line is the projection of the bicubic spline utilized for interpolation. Since $M_{\rm BH}$ is on a log scale, we include the $M_{\rm BH} = 0$ model at $M_{\rm BH} = 10^6\ M_\odot$.

## 5. THE INTERNAL DYNAMICS OF NGC 1023

In this section, we consider the implications for the internal structure of NGC 1023 that can be drawn from our data and modeling. In particular, Faber et al. (1997) suggested that NGC 1023 probably has a nuclear stellar disk, based on its surface photometry. Is this suggestion consistent with the dynamical structure seen in our best-fit model?

Figure 12 shows the internal dynamics of the best-fitting model. The three components of the internal velocity dispersion in this model are nearly isotropic at $r > 0''.4$ (19.6 pc). Within this radius as one approaches the nucleus, the anisotropy changes from radial anisotropy to tangential anisotropy in the central bin. This is indicated by $\sigma_r/\sigma_t < 1$ and $\sigma_\phi$ is much greater than $\sigma_r$ or $\sigma_\theta$ at the nucleus. This tangential anisotropy at the nucleus also suggests the pres-

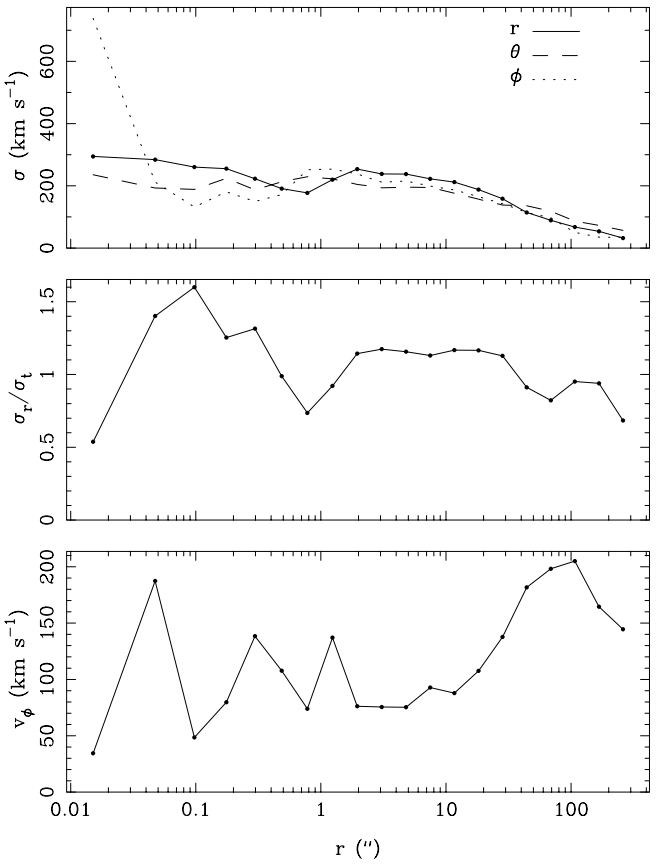


FIG. 12.—Internal dynamics along the major axis for the best-fitting model ($M_{\rm BH} = 5.6 \times 10^7\ M_\odot$, $M/L_V = 5.6$, and $i = 90°$). Starting from the top, the separate panels show the three internal velocity dispersions, the ratio of radial to tangential velocity dispersion [where $\sigma_t^2 = (\sigma_\theta^2 + \sigma_\phi^2)/2$], and $v_\phi$ (the mean velocity in the equatorial plane).

ence of a nuclear stellar disk. The low value of $v_\phi$ at the nucleus implies that the stars in this nuclear disk are nearly evenly divided between prograde and retrograde orbits.

The internal dynamics point to tangential anisotropy at the nucleus, which is normally associated with negative values of $h_4$ when projected onto the sky. However, the nuclear value of $h_4$ is significantly positive (Fig. 3), and the nuclear LOSVD has wings at velocities $\geq 600$ km s$^{-1}$ from systemic (Fig. 9). These strong tails likely indicate that, in addition to the population of stars in the nuclear disk, there are stars very close to the central BH with very large velocities (either radial or tangential) that are enhancing the wings of the nuclear LOSVD. This is consistent with the existence of a nuclear star cluster (§ 2.1) sufficiently bright to influence the central LOSVD.

Gebhardt et al. (2000a) and Ferrarese & Merritt (2000) have shown that, for galaxies with the best dynamical evidence for a BH, the mass of the BH is strongly correlated to the velocity dispersion $\sigma_e$ within the half-light radius $R_e$. NGC 1023, with a BH mass of $3.9 \times 10^7\ M_\odot$ and $\sigma_e = 205$ km s$^{-1}$, lies slightly below (with 2 $\sigma$ confidence) the ridge line of this relation. Although this offset is not significant, determining BH masses with comparable accuracy as NGC 1023 will probe the possible intrinsic scatter in this correlation. Given the observed high-velocity population of stars in the nucleus of NGC 1023, this galaxy is important since it may be one of the few galaxies where we actually observe the direct influence of the BH on the kinematics. Isolating this high-velocity nuclear population would provide even stronger constraints on the nuclear mass distribution.

We acknowledge several very useful suggestions from John Kormendy and Gregory Bothun. This work was supported by NASA Guaranteed Time Observer funding to the STIS Science Team.

REFERENCES

Barbon, R., & Capaccioli, M. 1975, A&A, 42, 103
Bender, R. 1990, A&A, 229, 441
Bender, R., Saglia, R. P., & Gerhard, O. E. 1994, MNRAS, 269, 785
Binney, J., & Tremaine, S. 1987, Galactic Dynamics (Princeton: Princeton Univ. Press)
de Vaucouleurs, G., et al. 1991, Third Reference Catalog of Bright Galaxies (Springer: New York)
Faber, S. M., et al. 1997, AJ, 114, 1771
Ferrarese, L., & Merritt, D. 2000, ApJ, 539, L9
Gebhardt, K., et al. 1996, AJ, 112, 105
———. 2000a, ApJ, 539, L13
———. 2000b, AJ, 119, 1157
Gerhard, O. E. 1993, MNRAS, 265, 213
Goudfrooij, P., Baum, S. A., & Walsh, J. R. 1997, in The 1997 *HST* Calibration Workshop, ed. S. Casertano et al. (Baltimore: STScI), 100
Kimble, R. A., et al. 1998, ApJ, 492, L83
Kormendy, J. 2000, in Galaxy Disks and Disk Galaxies, ed. J. G. Funes, S.J., & E. M. Corsini (San Francisco: ASP), in press (astro-ph/0007401)
Kormendy, J., & Bender, R. 1999, ApJ, 522, 772
Kormendy, J., & Richstone, D. 1995, ARA&A, 33, 581
Lauer, T. R., et al. 1995, AJ, 110, 2622
Lucy, L. B. 1974, AJ, 79, 745
Magorrian, J., et al. 1998, AJ, 115, 2285
Maoz, E. 1998, ApJ, 494, L181
Richardson, W. H. 1972, JOSA, 62, 55
Richstone, D., & Tremaine, S. 1988, ApJ, 327, 82
Richstone, D., et al. 1998, Nature, 395, A14
Schlegel, D. J., Finkbeiner, D. P., & Davis, M. 1998, ApJ, 500, 525
Schmidt, M., Schneider, D. P., & Gunn, J. E. 1995, AJ, 110, 68
Schwarzschild, M. 1979, ApJ, 232, 236
Simien, F., & de Vaucouleurs, G. 1986, ApJ, 302, 564
van der Marel, R. P., & Franx, M. 1993, ApJ, 407, 525
Woodgate, B. E., et al. 1998, PASP, 110, 1183